Highlights

A variably scaled moving least squares approach for improving resolution in magnetic resonance imaging

Mohammad Karimnejad Esfahani,Francesco Marchetti,Isabella Cama,Stefano De Marchi,Cristina Campi

- MLS with Variably Scaled Kernels (VSK) is proposed for MRI resolution enhancement.
- The MLS-VSK method improves edge preservation over standard interpolation methods.
- Theoretical error bounds for the MLS-VSK approximant are derived and analyzed.
- Tests on synthetic and real ADC MRI data show competitive reconstruction accuracy.
- Nearest-neighbor scaling outperforms linear scaling in sharpness index improvement.

A variably scaled moving least squares approach for improving resolution in magnetic resonance imaging

Mohammad Karimnejad Esfahani[a], Francesco Marchetti[b], Isabella Cama[c], Stefano De Marchi[d] and Cristina Campi[c,e,*]

[a]Dipartimento di Scienze Ambientali, Informatica e Statistica, Università Ca' Foscari, via Torino, 155, Mestre, 30172, Italy
[b]Dipartimento di Matematica "Tullio Levi-Civita", Università di Padova, via Trieste 63, Padova, 35121, Italy
[c]Dipartimento di Matematica, Università di Genova, via Dodecaneso 35, Genova, 16146, Italy
[d]Dipartimento di Medicina, Università di Padova, Via Giustiniani, 2, Padova, 35128, Italy
[e]IRCCS Azienda Ospedaliera Metropolitana, Largo Rosanna Benzi 10, Genova, 16132, Italy

ARTICLE INFO

Keywords:
moving least squares
variable-scaled kernels
magnetic resonance imaging
apparent diffusion coefficient

ABSTRACT

In this work, we investigate the reconstruction of low-resolution magnetic resonance images using the Moving Least Squares (MLS) method with low-degree polynomials, whose weights are set by using Variably Scaled Kernels (VSKs). The resulting MLS-VSK approach is first analyzed from a theoretical perspective and then tested in concrete experimental settings. Our tests show improvements in the reconstruction of higher-resolution images compared to other well-established image interpolation methods.

1. Introduction

Medical images exhibit varying spatial resolutions, depending on the imaging modality, scanner, acquisition protocol, and, in the case of Magnetic Resonance Imaging (MRI), sequences. Among the most promising and widely used MRI measurements, Apparent Diffusion Coefficient (ADC) provides information on the diffusivity of water molecules. It serves as a valuable biomarker in oncology, neurology, and stroke imaging. T1-weighted anatomical images, on the other hand, offer high spatial resolution and precise anatomical detail, which are essential for structural localization and region-of-interest (ROI) analysis. Integrating these two sequences would enable meaningful voxel-wise comparisons and multiparametric analysis. However, accurate spatial co-registration between ADC and T1-weighted images is non-trivial due to several factors. First, the acquisition methods for diffusion-weighted imaging (DWI), from which ADC maps are derived, are inherently susceptible to geometric distortions caused by eddy currents, susceptibility effects, and patient motion Arlinghaus, Welch, Chakravarthy, Xu, Farley, Abramson, Grau, Kelley, Mayer, Means-Powell, Meszoely, Gore and Yankeelov (2011). These distortions are often absent in the T1-weighted reference image, leading to spatial mismatches that can undermine both qualitative interpretation and quantitative analysis. Furthermore, the differences in image resolution, contrast polarity, and signal-to-noise ratio (SNR) between ADC and T1 images exacerbate the challenge of reliable alignment.

Traditional coregistration approaches typically rely on affine or deformable transformations to align diffusion-derived images with structural anatomy. Although affine registration can compensate for global translations and rotations, it often fails to correct localized non-linear distortions (e.g., near sinuses, skull base, or within the prostate). To address this, more advanced techniques, such as free-form deformation (FFD) Rueckert, Sonoda, Hayes, Hill, Leach and Hawkes (1999) and mutual information (MI)-driven alignment Woo, Stone and Prince (2015), have been employed. These methods have shown promising results in reducing spatial mismatch, particularly in contexts such as prostate cancer imaging, where lesion boundaries in ADC maps must be accurately overlaid onto anatomical landmarks for targeted biopsy or radiotherapy planning Hao, Huang, Gao, Chen and Wang (2017). An alternative strategy is to resample or warp T1-weighted images directly into diffusion space. This is particularly useful in neuro-oncology applications, such as glioblastoma imaging, where tumor segmentation from contrast-enhanced T1 scans can be propagated into ADC maps for diffusion-based tumor characterization Rydelius, Bengzon, Engelholm, Kinhult, Englund, Nilsson, Lätt, Lampinen and Sundgren (2023); Woodworth, Pope, Liau, Kim, Lai, Nghiemphu, Cloughesy

*Corresponding author
cristina.campi@unige.it (C. Campi)
ORCID(s):

and Ellingson (2014). Recently, to bypass the need for post hoc registration, quantitative imaging frameworks have been proposed that simultaneously acquire multiple parameter maps (e.g., T1, T2, and ADC) within a unified acquisition and reconstruction pipeline. These approaches, often based on MR fingerprinting (MRF) Panda, Obmann, Lo, Margevicius, Jiang, Schluchter, Patel, Nakamoto, Badve, Griswold, Jaeger, Ponsky and Gulani (2019) or MR multitasking Ma, Nguyen, Han, Wang, Deng, Binesh, Moser, Christodoulou and Li (2020), offer intrinsically coregistered outputs with high spatial resolution and significantly reduced scan time. Such techniques have demonstrated the ability to generate perfectly co-registered and distortion-free T1/T2/ADC maps in less than 10 minutes Ma et al. (2020), and other implementations using multidimensional MRF (mdMRF) can yield T1, T2, and ADC maps in as little as 24 seconds per slice Afzali, Mueller, Sakaie, Hu, Chen, Szczepankiewicz, Griswold, Jones and Ma (2022).

In many registration and reconstruction approaches, edge preservation represents an important aspect in the image processing pipeline. On the one hand, non-physical oscillations due to the well-known Gibbs phenomenon may appear when handling images containing sharp edges. On the other hand, treating the Gibbs phenomenon can easily lead to oversmoothed results, where the oscillations are reduced at the price of an unsatisfactory edge recovery. In the kernel-based approximation setting, the variably scaled framework has been largely considered in recent years to adapt the model with respect to the *shape* of the target function, including jumps and steep gradients. Taking advantage of the flexibility provided by radial kernel models, Variably Scaled Kernels (VSKs) Bozzini, Lenarduzzi, Rossini and Schaback (2015) substitute the lenghtscale parameter tuning with the choice of a scaling function, and have been effectively employed in various contexts Audone, Della Santa, Perracchione and Pieraccini (2025); Perracchione, Massone and Piana (2021); Marchetti, Perracchione, Volpara, Massone, De Marchi and Piana (2023). As a particular case, choosing a discontinuous scaling function allows a very accurate approximation of discontinuous target functions, in case the position of the jumps is well encoded in the scaling function. More in general, the results in Audone et al. (2025) indicate that the VSK approach benefits from a choice of scaling function that replicates the target signal.

The variably scaled approach has recently been introduced in the context of Moving Least Squares (MLS) in Karimnejad Esfahani, De Marchı and Marchetti (2023). The MLS method is a numerical technique that constructs smooth, continuous approximations. Unlike traditional least-squares methods that fit a single global function to all data points, MLS employs a local-fitting approach, solving a weighted least-squares problem around each evaluation point. The weights, typically defined by a smoothly decaying kernel function, assign a greater influence to nearby data points and fewer to distant ones. This property enables MLS to produce smooth approximations that adapt to local data variations (see (Fasshauer, 2007, Chap 22 & 23) or (Wendland, 2004, Chap 3 & 4)).

Initially introduced in the context of surface reconstruction and mesh-free methods in Lancaster and Salkauskas (1981), MLS has found widespread application in computational mechanics, computer graphics, and data interpolation (see, e.g., Levin (1998); Tey, Che Sidik, Asako, W Muhieldeen and Afshar (2021)). Its flexibility and ability to handle irregularly spaced data make it especially useful in meshless numerical schemes, such as the Element-Free Galerkin method. The main advantages of the method include high accuracy, smooth derivative behavior, and robustness to noise. However, it requires careful selection of weight functions and support domains to ensure stability and computational efficiency. Recently in Karimnejad Esfahani et al. (2023); Levin, Ramón, Ruiz-Alvarez and Yáñez (2025) the authors suggested selecting the weight functions so that they reflect the discontinuities in the target function that increase the accuracy of the recovery process in the non-smooth region.

In this paper, our purpose is to test the accuracy of MLS-VSK approaches to increase the resolution of ADC image series, with a particular focus on edge preservation. The proposed MLS-VSK approach reaches competitive performance compared to baseline image interpolation models, but in addition it is capable to better preserve the edges in the reconstructed images, as assessed in our numerical tests using sharpness index measure Zhu, Yu, Wang, Ke and Zhi (2023) among other metrics.

The paper is organized as follows: in Section 2 we recap the preliminary notions on both MRI and the basics of the approximation approach; in Section 3 we detail the proposed MLS-VSK approximant. Section 4 provides the details on the experimental setting, while in Section 5 we show the numerical results on low-resolution MR ADC images. Conclusions are given in Section 6.

2. Preliminaries

2.1. On MRI

MRI is a non-invasive imaging technique widely used in medicine to visualize anatomical structures. Its non-invasiveness makes it a leading tool for diagnostic and staging investigations in both oncological and neurodegenerative diseases. MRI exploits the magnetic properties of hydrogen nuclei, predominantly found in water molecules. When placed in a magnetic field, these nuclei align with the field, and a pulse of radiofrequency energy is applied to perturb their alignment. The hydrogen atoms return to their original state and emit signals, which are detected and converted into images. Applying different sequences of magnetic field gradients, radiofrequency pulses, and timing parameters produces different image types from the same magnetic resonance device. These distinct image types capture salient characteristics of the tissues and organs under investigation, and during an MRI examination, the patient undergoes sequences based on the protocol for the specific diagnostic question.

Among the most common types of MRI sequences we recall:

- T1-weighted (T1): Provides high-resolution images of anatomical structures. In brain imaging, it provides high-resolution images with clear contrast between gray matter, white matter, and surrounding tissues.
- T2-weighted (T2): This sequence highlights water-rich structures, making it highly effective for identifying lesions or abnormalities such as tumors, inflammation, or edema.
- Diffusion-Weighted Imaging (DWI): Measures the movement of water molecules in tissue, making it possible to identify areas of restricted diffusion, thanks to the application of gradients with different strengths b.

Figure 1 shows an example of the same brain slice using these three sequences.

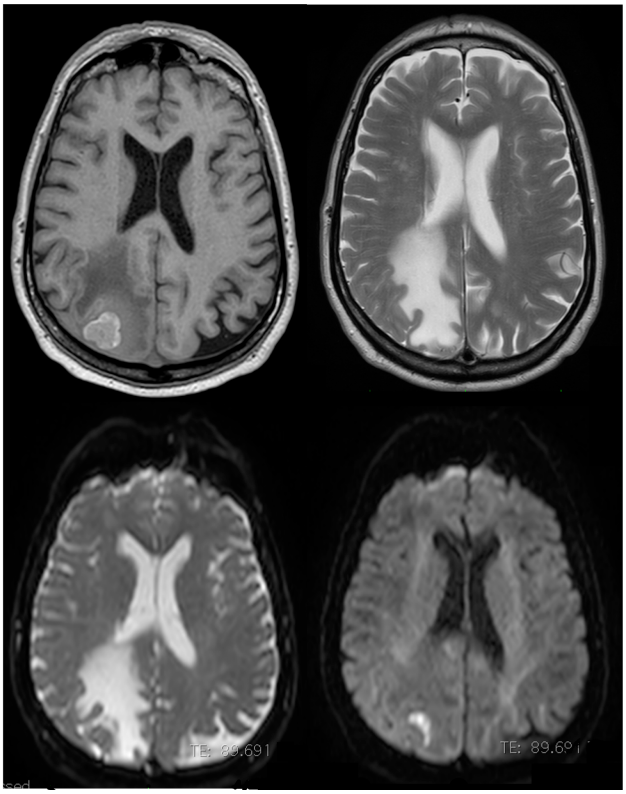

Figure 1: Top row, from left to right: T1 and T2 images; bottom row, from left to right: DWI images obtained with $b = 0$ and $b = 1000 s/mm^2$. These images are part of the CPTAC-CM collection National Cancer Institute Clinical Proteomic Tumor Analysis Consortium (CPTAC) (2018).

From DWI is possible to derive Apparent Diffusion Coefficient (ADC) images, using the DWI images acquired with two different b-values, thanks to the formula

$$ADC_b = \frac{\ln \frac{(DWI)_0}{(DWI)_b}}{b}$$

where DWI_0 is the DWI image acquired with a value of b equal to 0 and DWI_b is the DWI image acquired with a value of $b > 0$, i.e. not equal to 0.

Low ADC values typically correspond to restricted diffusion (e.g., in acute stroke or tumors), while high ADC values reflect more freely diffusing water (e.g., in normal brain tissue).

The parametric nature of ADC images makes them a powerful tool for quantitative tissue assessment, allowing comparisons between subjects and, within longitudinal studies, comparisons within the same subject. Consequently, DWI and ADC images are among the few MR sequences that produce parametric data. T1 images, although of paramount importance for identifying finer anatomical details, lack a physical encoding of grayscale tones, making it impossible to compare patients and quantitatively identify tissues within well-defined ranges. To this end, several sophisticated and computationally intensive methodologies have been proposed for image harmonization, among them we recall Caldera, Cavinato, Cappozzo, Cama, Garbarino, Cirone, Lodi, Tagliavini, Nigri, De Francesco, Ieva and Network (2025a); Caldera, Cavinato, Cirone, Cama, Garbarino, Lodi, Tagliavini, Nigri, Francesco, Cappozzo, Piana and Ieva (2025b); de Bruijne, Cattin, Cotin, Padoy, Speidel, Zheng and Essert (2021).

In clinical practice, physicians analyze different MR images together to capture the various aspects of the pathology. However, due to differences in spatial resolution and the varying physical meanings of voxel grayscale tones, it isn't easy to make quantitative assessments that combine the images.

The difference in spatial resolution, due to technical issues related to the application of the specific resonance sequences and the acquisition timing are evident in Figure 1. The voxel sizes of the images presented range from $0.49 \times 0.49 \times 1\ mm^3$ for T1 to $0.34 \times 0.34 \times 5\ mm^3$ for T2, up to $1.20 \times 1.20 \times 5\ mm^3$ for DWI.

2.2. From classical least squares to the moving least squares

Let $X = \{\mathbf{x}_1, \dots, \mathbf{x}_N\} \subset \Omega \subset \mathbb{R}^d$ be the given data sites, and $f \in C(\Omega)$ be an unknown function sampled at $\mathbf{f}_X = [f_1, \dots, f_N]^T$ with $f_i = f(\mathbf{x}_i)$ for all $1 \leq i \leq N$. The aim is to recover the function f based on the given function values. Methods used to do so must be stable and accurate with a reasonable computation cost. We formulate the approximation problem in a general finite-dimensional space $\mathcal{B} = \mathrm{span}\{b_1, \dots, b_q\}$, where $\{b_j\}_{j=1}^q$ is a prescribed basis. The approximant takes the form

$$s_{f,X}(\mathbf{x}) \;=\; \sum_{j=1}^{q} c_j\, b_j(\mathbf{x}) \;=\; \mathbf{b}(\mathbf{x})^T \mathbf{c}, \qquad \mathbf{x} \in \Omega, \tag{1}$$

where $\mathbf{b}(\mathbf{x}) = [b_1(\mathbf{x}), \dots, b_q(\mathbf{x})]^T$ and $\mathbf{c} \in \mathbb{R}^q$ is a coefficient vector to be determined. Let B denote the $N \times q$ collocation matrix with entries $B_{i,j} = b_j(\mathbf{x}_i)$; we assume throughout that $N \geq q$ and that B has full column rank.

Dating back to Legendre (1805), the simplest approach determines $\mathbf{c}$ by minimising the global residual

$$E^{\mathrm{GLS}} \;=\; \sum_{i=1}^{N} \left(s_{f,X}(\mathbf{x}_i) - f_i\right)^2 \;=\; \|B\mathbf{c} - \mathbf{f}\|_2^2.$$

The unique minimiser satisfies the normal equations

$$B^T B\, \mathbf{c} = B^T \mathbf{f} \qquad \Longrightarrow \qquad \mathbf{c} = (B^T B)^{-1} B^T \mathbf{f}. \tag{2}$$

In case the reliability of the observations varies across sites, one can introduce a diagonal weight matrix $W = \mathtt{diag}(w_1, \dots, w_N)$ with $w_i > 0$, and replaces (2) by

$$B^T W B\, \mathbf{c} = B^T W \mathbf{f} \qquad \Longrightarrow \qquad \mathbf{c} = (B^T W B)^{-1} B^T W \mathbf{f}. \tag{3}$$

The matrix $B^T W B$ is commonly referred to as the moment matrix.

For large data sets, fitting a single global element of $\mathcal{B}$ might be both ill-conditioned and computationally expensive. A natural remedy is to solve a separate weighted problem in a neighborhood of each evaluation point. However, in this case, there is no uniqueness in the approximate solution in any $\mathbf{x} \in \Omega$ due to overlapping of neighborhoods.

The Moving Least Squares (MLS) method resolves this ambiguity by requiring weights to continuously vary with $\mathbf{x}$ Lancaster and Salkauskas (1981). Formally, the MLS approximant is defined as

$$s_{f,X}(\mathbf{x}) \;=\; \operatorname*{argmin}_{g \in \mathcal{B}} \sum_{i=1}^{N} w(\mathbf{x}_i, \mathbf{x}) \left(g(\mathbf{x}_i) - f_i\right)^2, \tag{4}$$

which is induced by the weighted ℓ_2 inner product

$$\langle f, g \rangle_{w_{\mathbf{x}}} = \sum_{i=1}^{N} w_{\mathbf{x}}(\mathbf{x}_i)\, f(\mathbf{x}_i)\, g(\mathbf{x}_i),$$

where the weight $w_{\mathbf{x}}(\cdot) = w(\cdot, \mathbf{x})$ also depends on the evaluation point $\mathbf{x}$, hence the term moving. The local normal equations then read

$$B^T W B\, \mathbf{c}(\mathbf{x}) = B^T W(\mathbf{x})\mathbf{f} \qquad \Longrightarrow \qquad \mathbf{c}(\mathbf{x}) = \left(B^T W(\mathbf{x}) B\right)^{-1} B^T W(\mathbf{x})\mathbf{f}. \tag{5}$$

Substituting the solution of (5) into (1) yields the explicit representation

$$s_{f,X}(\mathbf{x}) \;=\; \sum_{i=1}^{N} \alpha_i(\mathbf{x})\, f_i,$$

where the generating functions (also called shape functions) $\alpha_i : \Omega \longrightarrow \mathbb{R}$ are given by

$$\boldsymbol{\alpha}(\mathbf{x})^T \;=\; \mathbf{b}(\mathbf{x})^T \left(B^T W(\mathbf{x}) B\right)^{-1} B^T W(\mathbf{x}). \tag{6}$$

The well-posedness of (5), and hence of the entire MLS scheme, requires the moment matrix $B^T W(\mathbf{x}) B$ to be positive definite.

Although the MLS framework is valid for any finite-dimensional approximation space $\mathcal{B}$, the remainder of this work is restricted to the case when $\mathcal{B} = \mathbb{P}_m^d$, i.e., the space of d-variate polynomials of total degree at most m, with basis $\{p_1, \ldots, p_q\}$ and $q = \binom{m+d}{d}$. We accordingly replace $\mathcal{B}$, $\{b_j\}$, $\mathbf{b}(\mathbf{x})$, and B by $\mathbb{P}_m^d$, $\{p_j\}$, $\mathbf{p}(\mathbf{x})$, and P throughout. This choice is motivated by the fact that low-degree polynomials are computationally cheap, and their approximation-theoretic properties are well-understood Wendland (2004); Fasshauer (2007). To investigate the well-posedness, error, and stability of the MLS method, one needs to impose conditions on the weight function.

Remark 1. *The influence of the data sites in the shape functions* (6) *is governed by the weight function, which vanishes for pairs $\mathbf{x}, \mathbf{x}_i \in \Omega$ with $\|\mathbf{x} - \mathbf{x}_i\| \geq h$. We therefore write $w(\mathbf{x}_i, \mathbf{x}) = \Phi(\mathbf{x}_i/h, \mathbf{x}/h)$ where $\Phi : \mathbb{R}^d \times \mathbb{R}^d \to \mathbb{R}$ is a positive definite radial kernel, $\Phi(\mathbf{x}_i, \mathbf{x}) = \varphi(\|\mathbf{x}_i - \mathbf{x}\|/h)$, with support in the unit ball $B(0,1)$ and positive on all of $B(0, \delta h)$ for $\delta \in (0,1]$. For what we have in mind, $\delta = 1$ is sufficient; however, in the literature, such as (Wendland, 2004, Chap 3 & 4) $\delta = 1/2$ is chosen. The well-known Wendland compactly supported radial kernels satisfy these conditions.*

Taking into account Remark 1, we let $I(\mathbf{x}) = \{1 < i < N : \|\mathbf{x} - \mathbf{x}_i\| < h\}$ be the family of indices of data points in the support of $w_{\mathbf{x}}$. So, the MLS approximant can be expressed as:

$$s_{f,X}(\mathbf{x}) = \sum_{i \in I(\mathbf{x})} \alpha_i(\mathbf{x}) f_i. \tag{7}$$

In this case, the well-posedness of the problem is guaranteed when the dataset has a quasi-uniform distribution and $\{\mathbf{x}_i : i \in I(\mathbf{x})\}$ is $\mathbb{P}_m^d$-unisolvent for any arbitrary $\mathbf{x} \in \Omega$. For the error and stability analysis of the MLS method, the following definitions are fundamental:

- The fill distance
$$h_{X,\Omega} = \sup_{\mathbf{x} \in \Omega} \min_{\mathbf{x}_i \in X} \|\mathbf{x} - \mathbf{x}_i\|,$$
- The separation distance
$$q_{X,\Omega} = \frac{1}{2} \min_{i \neq j} \|\mathbf{x}_i - \mathbf{x}_j\|.$$

For a detailed treatment of the MLS framework, we refer the reader to (Fasshauer, 2007, Chap. 22), (Wendland, 2004, Chap. 3 & 4). In practice, normal equations (5) (with $B = P$) are susceptible to numerical ill-conditioning, particularly when the data sites are nearly uniformly distributed. A stable solution is obtained by applying the QR decomposition to the weighted matrix $\sqrt{W(\mathbf{x})}\,P$. Writing $\sqrt{W(\mathbf{x})}\,P = QR$, with Q orthogonal and R upper triangular, we have:

$$\begin{aligned} P^T\sqrt{W(\mathbf{x})}\sqrt{W(\mathbf{x})}P\mathbf{c}(\mathbf{x}) &= P^T\sqrt{W(\mathbf{x})}\sqrt{W(\mathbf{x})}\mathbf{f}, \\ R^T\,Q^T\,Q\,R\mathbf{c}(\mathbf{x}) &= R^T\,Q^T\sqrt{W(\mathbf{x})}\mathbf{f}, \\ R\mathbf{c}(\mathbf{x}) &= Q^T\sqrt{W(\mathbf{x})}\mathbf{f}, \end{aligned}$$

which is solved by back-substitution and avoids squaring the condition number of P. We end this section by recalling that other common choices of the weight functions include globally supported Gaussian or Matérn radial basis functions (RBFs) that decay to zero as the distance from $\mathbf{x}$ increases. In the latter case, one selects a local neighborhood around $\mathbf{x}$, called the *stencil*, such that it encompasses n number of data points with $q \leq n < N$ and then solves (7) on the stencil corresponding to each evaluation point. We refer the reader to e.g. Bayona (2019); Mirzaei (2015, 2017) for more information on the MLS scheme.

2.3. Variably Scaled Kernels

To address the scattered data approximation problem considered in the previous section, another common approach consists of building the interpolant as a linear combination of RBFs. Given data sites X and corresponding function values, the RBF approximant takes the form

$$s_{f,X}(\mathbf{x}) = \sum_{i=1}^{N} c_i\,\Phi_\varepsilon(\mathbf{x},\mathbf{x}_i), \tag{8}$$

where $\Phi_\varepsilon(\mathbf{x},\mathbf{x}_i) = \varphi(\varepsilon\|\mathbf{x}-\mathbf{x}_i\|)$ such that, as in the construction of the weight function in the MLS framework, $\varphi : [0,\infty) \longrightarrow \mathbb{R}$ is a univariate function. The coefficients c_i are determined by imposing interpolation conditions $s_{f,X}(\mathbf{x}_j) = f_j$ for all $j = 1,\dots,N$.

The scalar $\varepsilon > 0$ is the shape parameter, and it governs the spatial scale of each basis function. Selecting an appropriate value of ε is a delicate task that has attracted considerable attention in the literature; see, e.g., Fasshauer (2007); Fasshauer and McCourt (2015). In the classical RBF setting, a single value of ε is applied uniformly across all translates of φ, meaning that the approximant adapts to the global scale of the data but cannot resolve local features such as steep gradients, discontinuities, or edges. A natural generalization is to allow ε to vary from one center to another, replacing the global shape parameter with a set of locally adapted values $\{\varepsilon_i\}_{i=1}^N$.

Although this idea is intuitive and has been explored empirically, it lacks a solid theoretical foundation: in particular, the positive definiteness of the resulting interpolation matrix is no longer guaranteed, and the solvability of the approximation problem may fail (cf. Fasshauer and McCourt (2015)).

The Variably Scaled Kernel (VSK) framework, first introduced in Bozzini et al. (2015), addresses this difficulty by mapping the d-dimensional approximation problem into $\mathbb{R}^{d+1}$. This is achieved by augmenting each data site $\mathbf{x}_i$ with an additional coordinate given by a scale function $\psi : \Omega \longrightarrow \mathbb{R}$, resulting in the scaled points $\Psi(\mathbf{x}_i) = (\mathbf{x}_i, \psi(\mathbf{x}_i)) \in \mathbb{R}^{d+1}$.

Definition 1 (Variably scaled kernel). *Given the kernel $\Phi : \Omega\times\Omega \longrightarrow \mathbb{R}$ and the scale function $\psi : \mathbb{R}^d \to \mathbb{R}^+$, the VSK $\Phi_\varepsilon^\psi : (\Omega\times\mathbb{R})\times(\Omega\times\mathbb{R}) \longrightarrow \mathbb{R}$ is defined as*

$$\Phi_\varepsilon^\psi(\mathbf{x},\mathbf{y}) = \Phi_\varepsilon\big((\mathbf{x},\psi(\mathbf{x})),(\mathbf{y},\psi(\mathbf{y}))\big), \tag{9}$$

Now, the VSK approximant can be rewritten as:

$$s_{f,X}(\mathbf{x}) = \sum_{i=1}^{N} c_i\Phi_\varepsilon^\psi(\mathbf{x},\mathbf{x}_i). \tag{10}$$

Because the underlying kernel Φ_ε remains a valid positive (semi-)definite kernel on $\mathbb{R}^{d+1}$, the VSK Φ_ε^ψ inherits positive (semi-)definiteness on $\mathbb{R}^d$ (cf. (Bozzini et al., 2015, Theorem 2.2)).

The key insight is that the scale function ψ plays the role of a spatially varying shape parameter, but preserving the positive definiteness of the interpolation matrix. When ψ is constant, the VSK reduces to a standard isotropic kernel. When ψ is chosen to mimic the local behavior of the target function f, for instance by being smooth where f is smooth and exhibiting rapid variation where f has steep gradients, the kernel adapts its effective support and anisotropy accordingly. A particularly important special case arises when ψ is a discontinuous function whose jumps includes those of f: the resulting Variably Scaled Discontinuous Kernels (VSDKs) have been shown to yield highly accurate approximations of discontinuous targets, since the lifted distance between points on opposite sides of a discontinuity becomes large, effectively decoupling the approximation across edges Campi, Marchetti and Perracchione (2021); De Marchi, Marchetti and Perracchione (2020b); De Marchi, Erb, Marchetti, Perracchione and Rossini (2020a).

In the next section, we study the adaptivity of the VSK setting in the MLS context, where ψ can modulate the weight function in the local least-squares problem.

3. The MLS-VSK approximant

The classical MLS scheme described in Section 2.2 constructs approximants whose local influence regions are determined entirely by the Euclidean distance between data sites and evaluation points. While this produces smooth reconstructions, but it carries a fundamental limitation in the presence of sharp transitions: the isotropic weight function averages data from both sides of an edge without distinction, systematically blurring the transition. The VSK framework recalled in Section 2.3 resolves the analogous problem for RBF interpolation by embedding the approximation domain into a higher-dimensional space through a scale function ψ. The central contribution of this section is to analyze the same adaptivity mechanism into the MLS setting in a rigorous and self-contained way.

Definition 2 (The scaled metric). *Let $\psi : \Omega \longrightarrow \mathbb{R}$ be a given scale function. We define the variably scaled distance*

$$d_\psi(\mathbf{x}, \mathbf{y}) \;:=\; \sqrt{\|\mathbf{x}-\mathbf{y}\|^2 + |\psi(\mathbf{x}) - \psi(\mathbf{y})|^2}, \qquad \mathbf{x}, \mathbf{y} \in \Omega. \tag{11}$$

Equation (11) is the Euclidean distance between the scaled points $(\mathbf{x}, \psi(\mathbf{x}))$ and $(\mathbf{y}, \psi(\mathbf{y}))$ in $\mathbb{R}^{d+1}$, and it coincides with the distance underlying the VSK framework of Section 2.3. Since it is induced by the Euclidean norm in $\mathbb{R}^{d+1}$, d_ψ is a genuine metric on Ω for any choice of ψ.

Let $\varphi : [0, \infty) \longrightarrow \mathbb{R}$ be a compactly supported, non-negative radial weight function satisfying the conditions of Remark 1 (e.g. a Wendland kernel). Given a support radius $h > 0$, we define the variably scaled weights

$$w^\Psi(\mathbf{x}_i, \mathbf{x}) \;:=\; \varphi\left(\frac{d_\psi(\mathbf{x}, \mathbf{x}_i)}{h}\right), \qquad i = 1, \dots, N. \tag{12}$$

When ψ is discontinuous, we observe that d_ψ assigns large distances across jumps of ψ, effectively decoupling the stencil on opposite sides of an edge, and assigning negligible weight to data points across a sharp intensity transition. Pointwise error estimates for discontinuous targets have been studied in Karimnejad Esfahani et al. (2023).

The MLS-VSK approximant is then defined by replacing the new weight (12) in the minimization problem (4):

$$s^\Psi_{f,X}(\mathbf{x}) \;=\; \underset{g \in \mathbb{P}^d_m}{\arg\min} \sum_{i=1}^{N} w^\Psi(\mathbf{x}_i, \mathbf{x}) \left(g(\mathbf{x}_i) - f_i\right)^2. \tag{13}$$

As in the standard MLS case, the solution of (13) admits the representation

$$s^\Psi_{f,X}(\mathbf{x}) \;=\; \sum_{i \in I^\Psi(\mathbf{x})} \alpha_i^\Psi(\mathbf{x})\, f_i, \tag{14}$$

where the shape functions $\alpha_i^\Psi : \Omega \longrightarrow \mathbb{R}$ satisfy the polynomial reproduction property

$$\sum_{i \in I^\Psi(\mathbf{x})} \alpha_i^\Psi(\mathbf{x})\, p(\mathbf{x}_i) \;=\; p(\mathbf{x}), \qquad \forall\, p \in \mathbb{P}^d_m, \quad \mathbf{x} \in \Omega. \tag{15}$$

Setting $W^\Psi(\mathbf{x})$ as a diagonal matrix carrying the weights, the shape functions are obtained from the local normal equations

$$P^T W^\Psi(\mathbf{x})\, P\, c^\Psi(\mathbf{x}) \;=\; P^T W^\Psi(\mathbf{x})\, \mathbf{f}. \tag{16}$$

The sufficient condition for unique solvability of (16) at a point $\mathbf{x}$ is equivalent to the positive definiteness of the moment matrix $P^T W^\psi(\mathbf{x})P$, which in turn requires the new stencil

$$I^\psi(\mathbf{x}) \ := \ \left\{1 \le i \le N \ : \ d_\psi(\mathbf{x}, \mathbf{x}_i) < h\right\} \tag{17}$$

to contain a $\mathbb{P}^d_m$-unisolvent subset of X. This is the only essential condition on ψ for the method to be well defined, and we isolate it in the following definition.

Definition 3 (Admissible scale function). *A function $\psi : \Omega \longrightarrow \mathbb{R}$ is called VSK-admissible for the data set X and support radius h if, for every $\mathbf{x} \in \Omega$, the stencil $I^\psi(\mathbf{x})$ defined in (17) contains a $\mathbb{P}^d_m$-unisolvent subset of X.*

3.1. With a bounded ψ

The following key lemma gives a quantitative comparison between metric and Euclidean neighborhoods, which will be used to verify admissibility in practice.

Lemma 1 (Metric-Euclidean ball comparison). *Let $\psi : \Omega \longrightarrow \mathbb{R}$ be such that $|\psi(\mathbf{x}) - \psi(\mathbf{y})| \le M$, for every $\mathbf{x} \in \Omega$ and $h > 0$. Then*

$$\|\mathbf{x} - \mathbf{y}\| \ \le \ d_\psi(\mathbf{x}, \mathbf{y}) \ \le \ \sqrt{\|\mathbf{x} - \mathbf{y}\|^2 + M^2}, \qquad \forall\, \mathbf{y} \in \Omega, \tag{18}$$

and consequently

$$B\big(\mathbf{x}, r_1\big) \ \subseteq \ B_{d_\psi}(\mathbf{x}, h) \ \subseteq \ B(\mathbf{x}, h)\,, \tag{19}$$

where $r_1 = \sqrt{\max(0,\, h^2 - M^2)}$ and $B_{d_\psi}(\mathbf{x}, h) := \{\mathbf{y} : d_\psi(\mathbf{x}, \mathbf{y}) < h\}$. In particular, if $h > M$, then $B_{d_\psi}(\mathbf{x}, h)$ contains the Euclidean ball $B(\mathbf{x}, r_1)$ of positive radius r_1.

Proof: The left inequality in (18) is immediate from definition (11). So,

$$d_\psi(\mathbf{x}, \mathbf{y})^2 = \|\mathbf{x} - \mathbf{y}\|^2 + |\psi(\mathbf{x}) - \psi(\mathbf{y})|^2 \le \|\mathbf{x} - \mathbf{y}\|^2 + M^2.$$

The ball inclusions (19) follow directly. □

Theorem 1 (Well-posedness of MLS-VSK). *Let $\Omega \subset \mathbb{R}^d$ be a bounded domain satisfying an interior cone condition, and let $X = \{\mathbf{x}_1, \ldots, \mathbf{x}_N\} \subset \Omega$ be quasi-uniform with fill distance $h_{X,\Omega}$ and separation distance q_X. Let $\psi : \Omega \longrightarrow \mathbb{R}$ be as in Lemma 1. Choose the support radius*

$$h \ > \ M + C_{\mathrm{uni}}\, h_{X,\Omega}, \tag{20}$$

where $C_{\mathrm{uni}} > 0$ depends only on d, m, and the quasi-uniformity constant of X. Then ψ is VSK-admissible (Definition 3), the moment matrix $P^T W^\psi(\mathbf{x})P$ is positive definite for every $\mathbf{x} \in \Omega$, and the MLS-VSK approximant $s^\psi_{f,X}$ is uniquely determined at every $\mathbf{x} \in \Omega$.

Proof: Fix $\mathbf{x} \in \Omega$. By Lemma 1 and condition (20), the metric ball $B_{d_\psi}(\mathbf{x}, h)$ contains the Euclidean ball $B(\mathbf{x}, r_1)$ with

$$r_1 = \sqrt{h^2 - M^2} > \sqrt{(M + C_{\mathrm{uni}} h_{X,\Omega})^2 - M^2} \ge C_{\mathrm{uni}}\, h_{X,\Omega}.$$

Since X is quasi-uniform, $X \cap B(\mathbf{x}, r_1)$ contains at least $\binom{m+d}{d}$ points in general position (by the interior cone condition), ensuring $\mathbb{P}^d_m$-unisolvency; see (Wendland, 2004, Ch. 4). Hence $I^\psi(\mathbf{x}) \supseteq X \cap B(\mathbf{x}, r_1)$ is $\mathbb{P}^d_m$-unisolvent. Since the weights are strictly positive on $I^\psi(\mathbf{x})$, the matrix $W^\psi(\mathbf{x})$ is positive definite on the relevant subspace, and standard arguments (Wendland, 2004, Ch. 3) give positive definiteness of $P^T W^\psi(\mathbf{x})P$ and unique solvability of (16). □

We note that Theorem 1 requires only a bounded ψ; so it applies directly to discontinuous choices, and in particular to the *nearest-neighbor* scale function we will consider in our numerical experiments.

Theorem 2 (Properties of MLS-VSK). *Under the assumptions of Theorem 1, there exist constants $C_1, C_2 > 0$, independent of $\mathbf{x}$ and $h_{X,\Omega}$, such that:*

(i) *Polynomial reproduction:* $\sum_{i\in I^\psi(\mathbf{x})} \alpha_i^\psi(\mathbf{x})\, p(\mathbf{x}_i) = p(\mathbf{x})$ *for all* $p \in \mathbb{P}_m^d$, $\mathbf{x} \in \Omega$.

(ii) *Stability:* $\sum_{i\in I^\psi(\mathbf{x})} |\alpha_i^\psi(\mathbf{x})| \le C_1$ *for all* $\mathbf{x} \in \Omega$.

(iii) *Locality:* $\alpha_i^\psi(\mathbf{x}) = 0$ *whenever* $\|\mathbf{x}-\mathbf{x}_i\| > C_2\, h_{X,\Omega}$.

Proof: The reproduction property follows directly from the constraints (15). For the property (ii), by Theorem 1 the stencil contains a $\mathbb{P}_m^d$-unisolvent set and the moment matrix is positive definite; quasi-uniformity gives a uniform upper bound on the stencil size via the right inclusion in (19). The classical stability estimate (Wendland, 2004, Ch. 4, Thm. 4.2) then yields the bound with C_1 independent of $\mathbf{x}$ and $h_{X,\Omega}$. The locality property is the immediate result of compact support of φ since $w^\Psi(\mathbf{x}_i,\mathbf{x}) = 0$ when $d_\psi(\mathbf{x},\mathbf{x}_i) \ge h$. The left inequality in (18) gives $d_\psi(\mathbf{x},\mathbf{x}_i) \ge \|\mathbf{x}-\mathbf{x}_i\|$, so $\alpha_i^\psi(\mathbf{x}) = 0$ for $\|\mathbf{x}-\mathbf{x}_i\| \ge h = C_2 h_{X,\Omega}$. □

3.2. With a Lipschitz continuous ψ

In what follows, we restrict ourselves to the case of Lipschitz continuous scale functions. Assuming ψ is Lipschitz continuous with constant $L > 0$, the bound in (18) sharpens to $d_\psi(\mathbf{x},\mathbf{y}) \le \sqrt{1+L^2}\,\|\mathbf{x}-\mathbf{y}\|$, and correspondingly

$$B\left(\mathbf{x},\ \frac{h}{\sqrt{1+L^2}}\right) \subseteq B_{d_\psi}(\mathbf{x},\ h) \subseteq B(\mathbf{x},\ h). \tag{21}$$

In this case, the metric and Euclidean balls are always comparable, regardless of the values of M and h. In the case where ψ is obtained via an interpolation process from the data $\{(\mathbf{x}_i, f_i)\}_{i=1}^N$, that is, ψ is any interpolant satisfying $\psi(\mathbf{x}_i) = f_i$ for all $i = 1,\dots,N$, we observe that L can be estimated as

$$L \ge \max_{i\neq j} \frac{|f_i - f_j|}{\|\mathbf{x}_i - \mathbf{x}_j\|}. \tag{22}$$

The following lemma paves the way for the error analysis of the MLS-VSK approximation under Lipschitz assumptions.

Lemma 2 (Quasi-uniformity of the scaled data set). *Let $\psi : \Omega \longrightarrow \mathbb{R}$ be Lipschitz continuous with constant $L > 0$, and define the scaled domain and data set*

$$\widetilde{\Omega} := \{(\mathbf{x},\psi(\mathbf{x})) : \mathbf{x}\in\Omega\} \subset \mathbb{R}^{d+1}, \qquad \widetilde{X} := \{(\mathbf{x}_i,\psi(\mathbf{x}_i)) : \mathbf{x}_i\in X\} \subset \mathbb{R}^{d+1}.$$

Then the separation distance $q_{\widetilde{X},\widetilde{\Omega}}$ and fill distance $h_{\widetilde{X},\widetilde{\Omega}}$ of $\widetilde{X}$ in $\widetilde{\Omega}$ satisfy

$$q_{X,\Omega} \le q_{\widetilde{X},\widetilde{\Omega}} \le \sqrt{1+L^2}\, q_{X,\Omega}, \tag{23}$$

$$h_{X,\Omega} \le h_{\widetilde{X},\widetilde{\Omega}} \le \sqrt{1+L^2}\, h_{X,\Omega}. \tag{24}$$

In particular, if X is quasi-uniform in Ω with constant $c > 0$, i.e. $q_{X,\Omega} \le h_{X,\Omega} \le c\, q_{X,\Omega}$, then $\widetilde{X}$ is quasi-uniform in $\widetilde{\Omega}$ with constant $c\sqrt{1+L^2}$.

Proof: For any two points $\mathbf{x},\mathbf{y}\in\Omega$, the Lipschitz condition gives $|\psi(\mathbf{x})-\psi(\mathbf{y})| \le L\|\mathbf{x}-\mathbf{y}\|$, so

$$\|\mathbf{x}-\mathbf{y}\| \le \sqrt{\|\mathbf{x}-\mathbf{y}\|^2 + |\psi(\mathbf{x})-\psi(\mathbf{y})|^2} \le \sqrt{1+L^2}\,\|\mathbf{x}-\mathbf{y}\|. \tag{25}$$

Recalling definition of the separation distance, and applying (25) to each pair $(\mathbf{x}_i,\mathbf{x}_j)$,

$$\tfrac{1}{2}\|\mathbf{x}_i-\mathbf{x}_j\| \le \tfrac{1}{2}\|(\mathbf{x}_i,\psi(\mathbf{x}_i)) - (\mathbf{x}_j,\psi(\mathbf{x}_j))\| \le \frac{\sqrt{1+L^2}}{2}\|\mathbf{x}_i-\mathbf{x}_j\|.$$

Taking the minimum over $i \neq j$ gives (23).

Recalling the definition of the fill distance, for any $(\mathbf{x}, \psi(\mathbf{x})) \in \widetilde{\Omega}$, applying (24) to the pair $(\mathbf{x}, \mathbf{x}_i)$,

$$\|\mathbf{x} - \mathbf{x}_i\| \;\leq\; \|(\mathbf{x}, \psi(\mathbf{x})) - (\mathbf{x}_i, \psi(\mathbf{x}_i))\| \;\leq\; \sqrt{1 + L^2}\,\|\mathbf{x} - \mathbf{x}_i\|,$$

which immediately concludes (24).

Eventally, if X is quasi-uniform with constant c from (23) and (24),

$$q_{\widetilde{X},\widetilde{\Omega}} \;\leq\; h_{\widetilde{X},\widetilde{\Omega}} \;\leq\; \sqrt{1 + L^2}\,h_{X,\Omega} \;\leq\; c\sqrt{1 + L^2}\,q_{X,\Omega} \;\leq\; c\sqrt{1 + L^2}\,q_{\widetilde{X},\widetilde{\Omega}},$$

so $\widetilde{X}$ is quasi-uniform in $\widetilde{\Omega}$ with constant $c\sqrt{1 + L^2}$. □

We are now ready for the following theorem.

Theorem 3 (Approximation error of MLS-VSK). *Let the assumptions of Theorem 2 hold, and suppose additionally that ψ is Lipschitz continuous with constant $L > 0$. Define Ω^* as the closure of $\bigcup_{\mathbf{x}\in\Omega} B(\mathbf{x}, C_2 h_{X,\Omega})$. If $f \in C^{m+1}(\Omega^*)$, then there exists a constant $C > 0$, depending only on d, m, L, and the constants of Theorem 2, such that*

$$\left| f(\mathbf{x}) - s^{\psi}_{f,X}(\mathbf{x}) \right| \;\leq\; C\, h^{m+1}_{X,\Omega}\, |f|_{C^{m+1}(\Omega^*)} \qquad \forall\, \mathbf{x} \in \Omega, \tag{26}$$

for all X with $h_{X,\Omega} < h_0$, where $|f|_{C^{m+1}(\Omega^*)} := \max_{|\alpha|=m+1} \|D^\alpha f\|_{L^\infty(\Omega^*)}$.

Proof: Under the Lipschitz assumption by Lemma 2 the scaled data set $\tilde{X} = \{(\mathbf{x}_i, \psi(\mathbf{x}_i))\}$ inherits quasi-uniformity from X with a modified constant. For any $\mathbf{x} \in \Omega$ and $p^* \in \mathbb{P}^d_m$,

$$f(\mathbf{x}) - s^{\psi}_{f,X}(\mathbf{x}) = \sum_{i\in I^{\psi}(\mathbf{x})} \alpha^{\psi}_i(\mathbf{x}) \left(f(\mathbf{x}_i) - p^*(\mathbf{x}_i) \right) - \left(f(\mathbf{x}) - p^*(\mathbf{x}) \right).$$

Choosing p^* as the degree-m Taylor polynomial of f at $\mathbf{x}$, bounding each term using the stability estimate of Theorem 2 (ii) and the locality property (iii), and applying standard polynomial approximation results (cf. (Wendland, 2004, Ch. 3, Thm. 3.2)) yields (26). □

When ψ is discontinuous, we note that the Lipschitz assumption of Theorem 3 fails, and the Taylor expansion argument no longer applies globally. Nevertheless, for smooth regions away from edges, Theorem 3 applies locally, with the stencil restricted to points on the same side of the discontinuity.

4. Experimental setting

4.1. ADC datasets

We provide some details on the two datasets that we consider in our numerical tests.

1) A generated synthetic (phantom) ADC map to serve as a controlled reference. This phantom was created based on average apparent diffusion coefficient (ADC) values reported in the literature for different anatomical regions of the human brain Naganawa, Sato, Katagiri, Mimura and Ishigaki (2003); Helenius, Soinne, Perkiö, Salonen, Kangasmäki, Kaste, Carano, Aronen and Tatlisumak (2002); Sener (2001). To define these regions, we relied on the FreeSurfer segmentation of a representative 'average' subject, the reference standard MNI152-T1-1mm Jenkinson, Bannister, Brady and Smith (2002), thereby ensuring that the spatial distribution of the simulated ADC values corresponded to realistic brain anatomy. The 3D phantom was generated using the following model:

$$phantom = \mu + \sigma \cdot randn(size(positions)), \tag{27}$$

where μ and σ are the mean and standard deviation of the normal distribution used to sample the voxel intensities, based on the ADC values derived from the literature. Variable positions define the spatial locations of the voxels belonging to each anatomical region.

2) For the real-world image, we employed an ADC image derived from the Human Connectome Project (HCP) dataset Van Essen, Ugurbil, Auerbach, Barch, Behrens, Bucholz, Chang, Chen, Corbetta, Curtiss, Della Penna, Feinberg, Glasser, Harel, Heath, Larson-Prior, Marcus, Michalareas, Moeller, Oostenveld, Petersen, Prior, Schlaggar, Smith, Snyder, Xu and Yacoub (2012). Specifically, we selected a subject from the Young Adult cohort, which consists of high-quality diffusion MRI acquisitions from healthy individuals.

Data type	Polynomial degree	Scale function	shape parameter
Synthetic data	1, 2, 3, 4	nearest neighbor	1, 50
	1, 2, 3, 4	linear interpolation	1, 50
ADC data	1, 2, 3, 4	nearest neighbor	1, 50
	1, 2, 3, 4	linear interpolation	1, 50

Table 1
Experiment parameters.

4.2. Model parameters

In our numerical experiments, the scale values ψ are set to be the 'nearest' or 'linear' interpolation for each evaluation point $\mathbf{x}$. To be more precise, for a given $\mathbf{x}$ (which is a new pixel in the recovered image), $\psi(\mathbf{x})$ is obtained using the MATLAB command interp2 with method = 'linear' or 'nearest'.

In all test problems, the following setting is fixed.

1) The size of the stencil $n = 2 \times q$ where q is the dimension of the polynomial space.

2) The linear Matérn RBF as the weight function without any regularization term in the weight matrix W.

The parameters used in the numerical experiments are in Table 1. The choice of the shape parameter value $\varepsilon = 1$ or $\varepsilon = 50$ is representative to evaluate two different scenarios: *wide* or *narrow* basis functions.

4.3. Image quality metrics

To provide a quantitative evaluation of our proposed method, we use the following metrics to compare MLS-VSK with the standard MLS, piecewise linear, and cubic interpolation methods.

1) The **root mean squared error (RMSE)** measures the average pixel deviation between the reconstructed and reference images, providing a quantitative assessment of the overall fidelity.

2) The **Total Variation (TV)** measures how much the image intensity changes overall - it is the sum of absolute gradients across all pixels. Originally, in Strong and Chan (2003); Rudin, Osher and Fatemi (1992), TV minimization was used for image denoising; however, excessive TV minimization often leads to oversmoothing and loss of fine details, resulting in visually blurred reconstructions. Therefore, a higher TV value does not necessarily indicate poorer reconstruction quality; rather, it may correspond to better preservation of textures and edges, as demonstrated in our numerical experiments.

3) The **Sharpness Index (SI)** that quantifies the degree of edge definition and fine-detail clarity within an image. Unlike RMSE, which requires a reference image, SI can be computed directly from the reconstructed image. It measures the strength of local intensity variations—higher SI values indicate sharper, more detailed images, whereas lower values correspond to blurred or overly smooth reconstructions. See, e.g., Zhu et al. (2023) for an overview of the sharpness index.

5. Results

The MATLAB implementation used in this work is publicly available at `https://github.com/cristinacampi/MLS_VSK_MRI`.

5.1. Synthetic data

We first consider a synthetic dataset that mimics the real data of interest, i.e., MR images of the brain, comprising 78 slices (see Subsection 4). Figure 2 shows, in the first row, one of the original images (left panel) and its downsampled version (right panel), and in the second and third rows, the reconstructed image using the four methods with nearest neighbor as scale function.

In Table 2, the metrics evaluating the reconstructions with $\epsilon = 50$, degree = 3, and nearest neighbors as scale function. w.r.t. the corresponding original images, averaged over 78 images composing the 3D volume. The results using all the parameters in Table 1 are in A, Table 4.

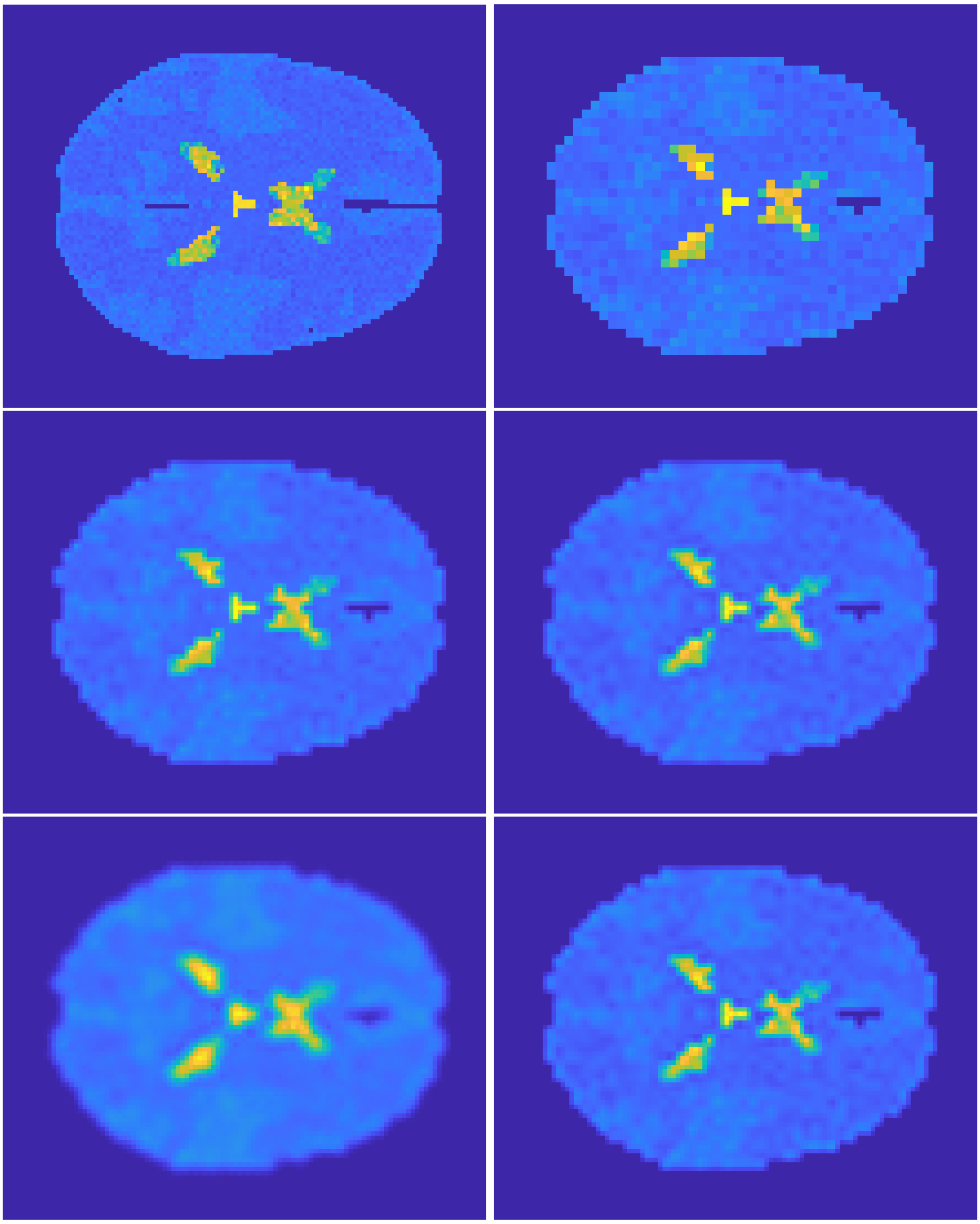

Figure 2: Synthetic dataset, slice 45, $\epsilon = 50$, degree $= 3$, nearest neighbors as scale function. First row: the original image (left) and its downsampled version. Second row: Reconstructions with Linear (left) and Cubic (right) interpolation. Third row: Reconstructions with MLS (left) and MLS-VSK (right).

5.2. ADC data

We also test the method on a real dataset comprising 96 images. Figure 3 shows in the first row one of the original images (left panel) and its downsampled version (right panel), and in the second and third rows the reconstructed image using the four methods with nearest neighbor as scale function. In Table 3, the metrics evaluating the reconstructions with $\epsilon = 50$, degree $= 3$, and nearest neighbors as scale function. w.r.t. the corresponding original images, averaged over 96 images comprising the 3D volume. The results using all the parameters in Table 1 are in A, Table 5.

	RMSE	TV	SI
Linear	0.000106 $\pm$ 0.000039	0.515 $\pm$ 0.271	262.285 $\pm$ 172.979
Cubic	0.000108 $\pm$ 0.000039	0.569 $\pm$ 0.304	234.094 $\pm$ 158.804
MLS	0.000113 $\pm$ 0.000041	0.427 $\pm$ 0.221	80.467 $\pm$ 87.743
MLS-VSK	0.000108 $\pm$ 0.000039	0.567 $\pm$ 0.303	235.261 $\pm$ 159.326

Table 2
Synthetic dataset. Average $\pm$ deviation standard on 78 reconstructed images with respect to the original ones with Linear, Cubic, MLS-VSK, and MLS. The scale function for MLS-VSK is the nearest neighbor while ϵ is 50 and degree is 3.

	RMSE	TV	SI
Linear	0.000267 $\pm$ 0.000036	3.387 $\pm$ 0.563	91.659 $\pm$ 30.807
Cubic	0.000276 $\pm$ 0.000038	4.176 $\pm$ 0.708	112.029 $\pm$ 41.552
MLS	0.000276 $\pm$ 0.000038	2.745 $\pm$ 0.453	32.067 $\pm$ 13.672
MLS-VSK	0.000285 $\pm$ 0.000039	4.693 $\pm$ 0.795	236.513 $\pm$ 71.349

Table 3
ADC dataset. Average $\pm$ deviation standard on 96 reconstructed images with respect to the original ones with Linear, Cubic, MLS-VSK, and MLS. The scale function for MLS-VSK is the nearest neighbor, while ϵ is 50 and the degree is 3.

6. Discussion and Conclusions

In this work, we proposed a MLS approach incorporating VSK for the recovery and interpolation of MRI data, with a specific focus on low-resolution ADC maps. By integrating the scale function within the MLS weighting kernel, our approach adapts to local image structures. It preserves edge information, effectively mitigating the excessive smoothness typically observed in conventional MLS reconstructions. Quantitative evaluations based on RMSE, TV, and SI demonstrated that MLS-VSK produces sharper images with better preservation of anatomical details, while maintaining reconstruction fidelity comparable to standard MLS approaches. Although the interpolated images remain low-resolution, visual inspection corroborated these findings, showing that MLS-VSK suppresses oversmoothing and enhances structural consistency across reconstructed images.

The theoretical framework developed holds for any VSK-admissible scale function ψ (see Definition 3). The error estimate of Theorem 3 holds for any fixed Lipschitz continuous ψ, but it does not capture the qualitative advantage of a well-chosen scale function. The reconstruction error at a point $\mathbf{x}$ near an edge is controlled by how well the local polynomial fits f on the scaled stencil $I^{\Psi}(\mathbf{x})$: the fit is accurate when all stencil points lie on the same smooth piece of f as $\mathbf{x}$, and degrades when the stencil contains points from the opposite side of the edge. Having the ideal choice $\psi = f$ unavailable, among computable choices, the nearest-neighbor interpolant satisfies $\psi(\mathbf{x}_i) = f_i$ at every data node and is piecewise constant with jumps approximately aligned with those of f. This provides an empirical justification for the superiority of the nearest-neighbor scaling observed in Section 5.

Despite its promising performance, several aspects of the proposed methods require further investigation: First, we assumed a fixed polynomial degree and a predefined scale function, which may limit flexibility in heterogeneous anatomical regions. Adaptive strategies for selecting these parameters based on local image features or data-driven optimization could further enhance reconstruction quality. Second, while we focused on ADC data in the present study, extending the MLS-VSK approach to multimodal MRI fusion (e.g., T1/T2/ADC integration) would be a challenging test of the method's ability to recover complementary information across modalities simultaneously.

Finally, the MLS-VSK formulation can be interpreted as a classical MLS approximation equipped with an anisotropic kernel induced by the scale function, and shares some common traits with MLS schemes with anisotropic kernels or spatially varying supports, where both the support radius and the underlying metric depend on the evaluation point. Such approaches fall outside the classical MLS theory developed in Wendland (2004); Mirzaei (2015), but they may contribute to the development of new theoretical foundations for MLS methods, both for function recovery and for the meshfree discretization of partial differential equations.

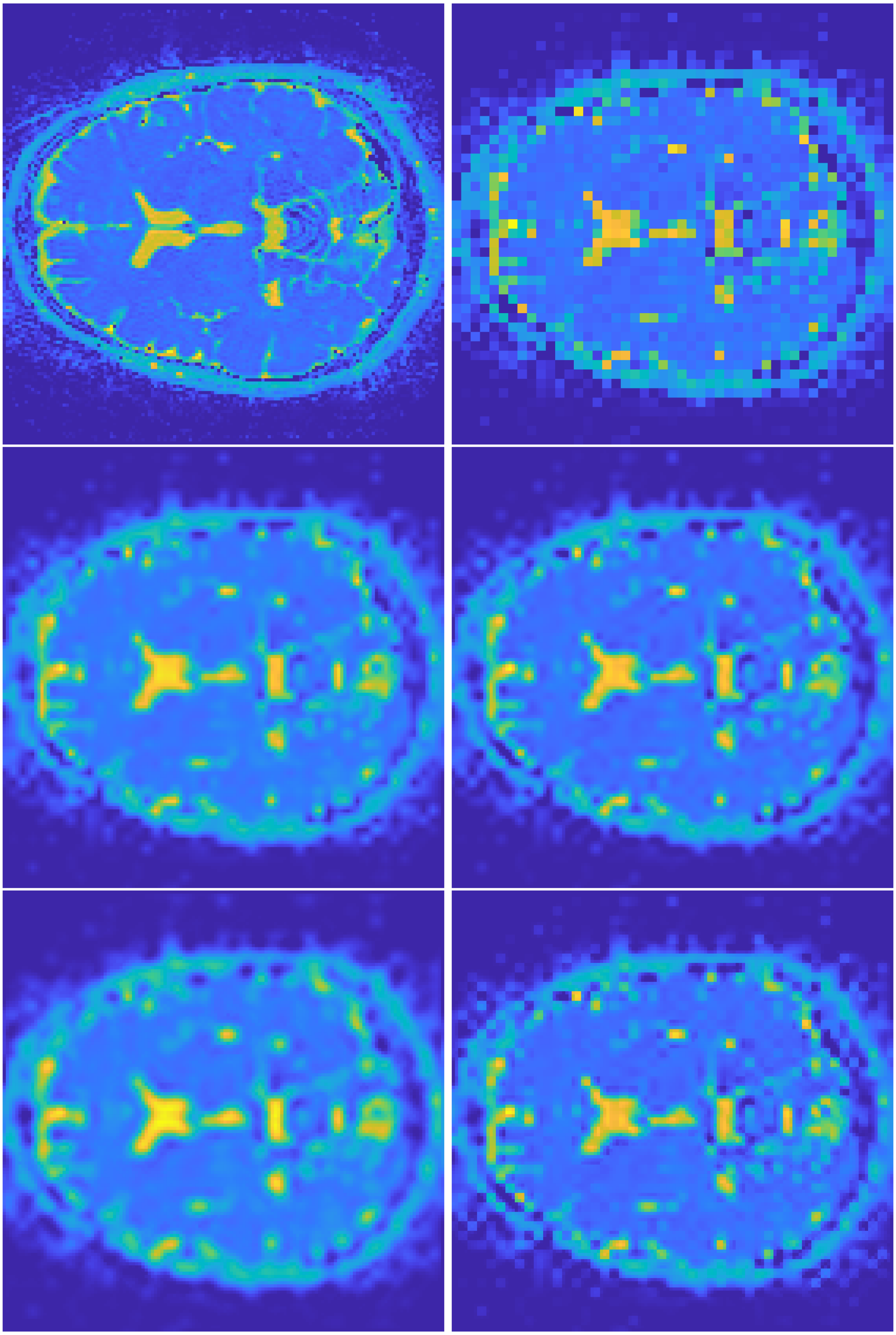

Figure 3: ADC dataset, image 40, $\epsilon = 50$, degree = 3, nearest neighbors as scale function. First row: the original image (left) and its downsampled version. Second row: Reconstructions with Linear(left) and Cubic (right) interpolation. Third row: Reconstructions with MLS (left) and MLS-VSK (right).

	RMSE	TV	SI
Linear	0.000106 ± 0.000039	0.515 ± 0.271	262.285 ± 172.979
Cubic	0.000108 ± 0.000039	0.569 ± 0.304	234.094 ± 158.804
MLS $\epsilon = 1$, degree = 1	0.000126 ± 0.000047	0.377 ± 0.191	108.205 ± 180.972
MLS $\epsilon = 1$, degree = 2	0.000119 ± 0.000044	0.485 ± 0.257	148.279 ± 153.691
MLS $\epsilon = 1$, degree = 3	0.000124 ± 0.000047	0.419 ± 0.217	70.864 ± 90.069
MLS $\epsilon = 1$, degree = 4	0.000119 ± 0.000045	0.495 ± 0.261	86.829 ± 94.982
MLS $\epsilon = 50$, degree = 1	0.000118 ± 0.000044	0.383 ± 0.195	85.977 ± 128.289
MLS $\epsilon = 50$, degree = 2	0.000110 ± 0.000040	0.488 ± 0.258	136.793 ± 122.896
MLS $\epsilon = 50$, degree = 3	0.000113 ± 0.000041	0.427 ± 0.221	80.467 ± 87.743
MLS $\epsilon = 50$, degree = 4	0.000110 ± 0.000040	0.497 ± 0.261	106.814 ± 97.197
MLS-VSK $\epsilon = 1$, degree = 1, linear	0.000117 ± 0.000043	0.384 ± 0.195	86.306 ± 127.167
MLS-VSK $\epsilon = 1$, degree = 1, nearest	0.000117 ± 0.000043	0.384 ± 0.195	86.306 ± 127.167
MLS-VSK $\epsilon = 1$, degree = 2, linear	0.000110 ± 0.000040	0.490 ± 0.259	139.015 ± 122.867
MLS-VSK $\epsilon = 1$, degree = 2, nearest	0.000110 ± 0.000040	0.490 ± 0.259	139.015 ± 122.867
MLS-VSK $\epsilon = 1$, degree = 3, linear	0.000112 ± 0.000041	0.429 ± 0.223	84.001 ± 90.756
MLS-VSK $\epsilon = 1$, degree = 3, nearest	0.000112 ± 0.000041	0.429 ± 0.223	84.001 ± 90.756
MLS-VSK $\epsilon = 1$, degree = 4, linear	0.000109 ± 0.000040	0.499 ± 0.263	111.329 ± 99.956
MLS-VSK $\epsilon = 1$, degree = 4, nearest	0.000109 ± 0.000040	0.499 ± 0.263	111.329 ± 99.956
MLS-VSK $\epsilon = 50$, degree = 1, linear	0.000106 ± 0.000039	0.515 ± 0.271	262.285 ± 172.979
MLS-VSK $\epsilon = 50$, degree = 1, nearest	0.000106 ± 0.000039	0.515 ± 0.271	262.285 ± 172.979
MLS-VSK $\epsilon = 50$, degree = 2, linear	0.000108 ± 0.000040	0.570 ± 0.304	243.374 ± 166.634
MLS-VSK $\epsilon = 50$, degree = 2, nearest	0.000108 ± 0.000039	0.570 ± 0.304	242.916 ± 162.989
MLS-VSK $\epsilon = 50$, degree = 3, linear	0.000108 ± 0.000039	0.567 ± 0.303	235.261 ± 159.326
MLS-VSK $\epsilon = 50$, degree = 3, nearest	0.000108 ± 0.000039	0.567 ± 0.303	235.261 ± 159.326
MLS-VSK $\epsilon = 50$, degree = 4, linear	0.000108 ± 0.000039	0.567 ± 0.303	235.289 ± 159.319
MLS-VSK $\epsilon = 50$, degree = 4, nearest	0.000108 ± 0.000039	0.567 ± 0.303	235.289 ± 159.319

Table 4
Synthetic dataset. Average ± deviation standard on 78 reconstructed images with respect to the original ones with Linear, Cubic, MLS-VSK, and MLS.

Acknowledgments

MKE, SDM and CC acknowledge the financial support under the National Recovery and Resilience Plan (NRRP), Mission 4, Component 2, Investment 1.1, Call for tender No. 104 published on 2.2.2022 by the Italian Ministry of University and Research (MUR), funded by the European Union – NextGenerationEU– Project Title "Computational mEthods for Medical Imaging (CEMI)" – CUP D53D23005830006 - Grant Assignment Decree No. 973 adopted on 30.6.2023 by the Italian Ministry of University and Research (MUR).

A. Additional results

References

Afzali, M., Mueller, L., Sakaie, K., Hu, S., Chen, Y., Szczepankiewicz, F., Griswold, M.A., Jones, D.K., Ma, D., 2022. MR fingerprinting with b-tensor encoding for simultaneous quantification of relaxation and diffusion in a single scan. Magnetic resonance in medicine 88, 2043–2057. doi:doi:10.1002/mrm.29352.

Arlinghaus, L.R., Welch, E.B., Chakravarthy, A.B., Xu, L., Farley, J.S., Abramson, V.G., Grau, A.M., Kelley, M.C., Mayer, I.A., Means-Powell, J.A., Meszoely, I.M., Gore, J.C., Yankeelov, T.E., 2011. Motion correction in diffusion-weighted mri of the breast at 3t. Journal of Magnetic Resonance Imaging 33, 1063–1070. doi:10.1002/jmri.22562.

Audone, G., Della Santa, F., Perracchione, E., Pieraccini, S., 2025. A recipe for learning variably scaled kernels via discontinuous neural networks. Journal of Computational and Applied Mathematics 469. doi:10.1016/j.cam.2025.116653.

Bayona, V., 2019. Comparison of moving least squares and RBF+ poly for interpolation and derivative approximation. Journal of Scientific Computing 81, 486–512. doi:10.1007/s10915-019-01028-8.

Bozzini, M., Lenarduzzi, L., Rossini, M., Schaback, R., 2015. Interpolation with variably scaled kernels. IMA Journal of Numerical Analysis 35, 199–219. doi:10.1093/imanum/drt071.

	RMSE	TV	SI
Linear	0.000267 ± 0.000036	3.387 ± 0.563	91.659 ± 30.807
Cubic	0.000276 ± 0.000038	4.176 ± 0.708	112.029 ± 41.552
MLS, $\epsilon = 1$, degree = 1	0.000293 ± 0.000040	2.315 ± 0.365	52.659 ± 21.076
MLS, $\epsilon = 1$, degree = 2	0.000279 ± 0.000038	3.224 ± 0.541	65.613 ± 25.551
MLS, $\epsilon = 1$, degree = 3	0.000291 ± 0.000040	2.644 ± 0.430	32.285 ± 14.206
MLS, $\epsilon = 1$, degree = 4	0.000283 ± 0.000039	3.164 ± 0.531	42.325 ± 19.531
MLS, $\epsilon = 50$, degree = 1	0.000282 ± 0.000038	2.356 ± 0.376	41.580 ± 15.977
MLS, $\epsilon = 50$, degree = 2	0.000269 ± 0.000037	3.296 ± 0.554	54.129 ± 22.064
MLS, $\epsilon = 50$, degree = 3	0.000276 ± 0.000038	2.745 ± 0.453	32.067 ± 13.672
MLS, $\epsilon = 50$, degree = 4	0.000270 ± 0.000037	3.286 ± 0.555	43.200 ± 19.253
MLS-VSK, $\epsilon = 1$, degree = 1, linear	0.000278 ± 0.000038	2.404 ± 0.385	40.202 ± 15.227
MLS-VSK, $\epsilon = 1$, degree = 1, nearest	0.000278 ± 0.000038	2.404 ± 0.385	40.202 ± 15.227
MLS-VSK, $\epsilon = 1$, degree = 2, linear	0.000267 ± 0.000036	3.370 ± 0.567	55.257 ± 22.643
MLS-VSK, $\epsilon = 1$, degree = 2, nearest	0.000267 ± 0.000036	3.370 ± 0.567	55.257 ± 22.643
MLS-VSK, $\epsilon = 1$, degree = 3, linear	0.000272 ± 0.000037	2.841 ± 0.471	35.248 ± 14.733
MLS-VSK, $\epsilon = 1$, degree = 3, nearest	0.000272 ± 0.000037	2.841 ± 0.471	35.248 ± 14.733
MLS-VSK, $\epsilon = 1$, degree = 4, linear	0.000268 ± 0.000036	3.403 ± 0.575	49.037 ± 21.081
MLS-VSK, $\epsilon = 1$, degree = 4, nearest	0.000268 ± 0.000036	3.403 ± 0.575	49.037 ± 21.081
MLS-VSK, $\epsilon = 50$, degree = 1, linear	0.000271 ± 0.000037	3.438 ± 0.574	99.298 ± 34.421
MLS-VSK, $\epsilon = 50$, degree = 1, nearest	0.000271 ± 0.000037	3.438 ± 0.574	99.298 ± 34.421
MLS-VSK, $\epsilon = 50$, degree = 2, linear	0.000284 ± 0.000038	4.696 ± 0.796	232.275 ± 69.847
MLS-VSK, $\epsilon = 50$, degree = 2, nearest	0.000284 ± 0.000038	4.696 ± 0.796	232.277 ± 69.854
MLS-VSK, $\epsilon = 50$, degree = 3, linear	0.000285 ± 0.000039	4.693 ± 0.795	236.512 ± 71.348
MLS-VSK, $\epsilon = 50$, degree = 3, nearest	0.000285 ± 0.000039	4.693 ± 0.795	236.513 ± 71.349
MLS-VSK, $\epsilon = 50$, degree = 4, linear	0.000284 ± 0.000038	4.659 ± 0.788	228.820 ± 70.041
MLS-VSK, $\epsilon = 50$, degree = 4, nearest	0.000284 ± 0.000038	4.659 ± 0.788	228.819 ± 70.040

Table 5
ADC dataset. Average ± deviation standard on 96 reconstructed images with respect to the original ones with Linear, Cubic, MLS-VSK, and MLS.

de Bruijne, M., Cattin, P.C., Cotin, S., Padoy, N., Speidel, S., Zheng, Y., Essert, C. (Eds.), 2021. Style Transfer Using Generative Adversarial Networks for Multi-site MRI Harmonization, Springer International Publishing. doi:10.1007/978-3-030-87199-4-30.

Caldera, L., Cavinato, L., Cappozzo, A., Cama, I., Garbarino, S., Cirone, A., Lodi, R., Tagliavini, F., Nigri, A., De Francesco, S., Ieva, F., Network, R.N., 2025a. Disarm: Disentangled scanner-free image generation via unsupervised image2image translation, in: Bathula, D.R., Benet Nirmala, A., Dvornek, N.C., Govindarajan, S.T., Habes, M., Kumar, V., Nebli, A., Wolfers, T., Xiao, Y. (Eds.), Machine Learning in Clinical Neuroimaging, Springer Nature Switzerland, Cham. pp. 102–112. doi:10.1007/978-3-031-78761-4-10.

Caldera, L., Cavinato, L., Cirone, A., Cama, I., Garbarino, S., Lodi, R., Tagliavini, F., Nigri, A., Francesco, S.D., Cappozzo, A., Piana, M., Ieva, F., 2025b. Disarm++: Beyond scanner-free harmonization. doi:10.48550/arXiv.2505.0371, arXiv:2505.03715.

Campi, C., Marchetti, F., Perracchione, E., 2021. Learning via variably scaled kernels. Advances in Computational Mathematics 47, 51. doi:10.1007/s10444-021-09875-6.

De Marchi, S., Erb, W., Marchetti, F., Perracchione, E., Rossini, M., 2020a. Shape-driven interpolation with discontinuous kernels: Error analysis, edge extraction, and applications in magnetic particle imaging. SIAM Journal on Scientific Computing 42, B472–B491.

De Marchi, S., Marchetti, F., Perracchione, E., 2020b. Jumping with variably scaled discontinuous kernels (VSDKs). BIT Numerical Mathematics 60, 441–463. doi:10.1007/s10543-019-00786-z.

De Marchi, S., Martínez, A., Perracchione, E., 2019a. Fast and stable rational RBF-based partition of unity interpolation. Journal of Computational and Applied Mathematics 349, 331–343. doi:10.1016/j.cam.2018.07.020.

De Marchi, S., Martinez, A., Perracchione, E., Rossini, M., 2019b. Rbf-based partition of unity methods for elliptic pdes: Adaptivity and stability issues via variably scaled kernels. Journal of scientific computing 79, 321–344.

Fasshauer, G., McCourt, M., 2015. Kernel-based Approximation Methods using MATLAB. WORLD SCIENTIFIC. URL: https://www.worldscientific.com/doi/abs/10.1142/9335, doi:10.1142/9335, arXiv:https://www.worldscientific.com/doi/pdf/10.1142/9335.

Fasshauer, G.E., 2007. Meshfree Approximation Methods with MATLAB. World Scientific Pub Co Inc.

Hao, L., Huang, Y., Gao, Y., Chen, X., Wang, P., 2017. Nonrigid registration of prostate diffusion-weighted mri. Journal of Healthcare Engineering 2017, 9296354. doi:10.1155/2017/9296354.

Helenius, J., Soinne, L., Perkiö, J., Salonen, O., Kangasmäki, A., Kaste, M., Carano, R.A.D., Aronen, H.J., Tatlisumak, T., 2002. Diffusion-weighted mr imaging in normal human brains in various age groups. American Journal of Neuroradiology 23, 194–199.

Hwang, S.I., Ahn, H., Lee, H.J., Hong, S.K., Byun, S.S., Lee, S., Choe, G., Park, J.S., Son, Y., 2021. Comparison of accuracies between real-time nonrigid and rigid registration in the MRI–US fusion biopsy of the prostate. Diagnostics 11. doi:10.3390/diagnostics11081481.

Jenkinson, M., Bannister, P., Brady, M., Smith, S., 2002. Improved optimization for the robust and accurate linear registration and motion correction of brain images. Neuroimage 17, 825–841. doi:10.1006/nimg.2002.1132.

Karimnejad Esfahani, M., De Marchı, S., Marchetti, F., 2023. Moving least squares approximation using variably scaled discontinuous weight function. Constructive Mathematical Analysis 6, 38–54. doi:10.33205/cma.1247239.

Lancaster, P., Salkauskas, K., 1981. Surfaces generated by moving least squares methods. Mathematics of computation 37, 141–158.

Levin, D., 1998. The approximation power of moving least-squares. Mathematics of computation 67, 1517–1531. doi:10.1090/S0025-5718-98-00974-0.

Levin, D., Ramón, J.M., Ruiz-Alvarez, J., Yáñez, D.F., 2025. Data-dependent moving least squares. Applied Numerical Mathematics doi:10.1016/j.apnum.2025.05.002.

Ma, S., Nguyen, C.T., Han, F., Wang, N., Deng, Z., Binesh, N., Moser, F.G., Christodoulou, A.G., Li, D., 2020. Three-dimensional simultaneous brain T_1, T_2, and adc mapping with mr multitasking. Magnetic Resonance in Medicine 84, 72–88. doi:10.1002/mrm.28092.

Marchetti, F., Perracchione, E., Volpara, A., Massone, A.M., De Marchi, S., Piana, M., 2023. Mapped variably scaled kernels: Applications to solar imaging, in: Gervasi, O., Murgante, B., Rocha, A.M.A.C., Garau, C., Scorza, F., Karaca, Y., Torre, C.M. (Eds.), Computational Science and Its Applications – ICCSA 2023 Workshops, Springer Nature Switzerland, Cham. pp. 577–592.

Mirzaei, D., 2015. Analysis of moving least squares approximation revisited. Journal of Computational and Applied Mathematics 282, 237–250. doi:10.1016/j.cam.2015.01.007.

Mirzaei, D., 2017. Direct approximation on spheres using generalized moving least squares. BIT Numerical Mathematics 57, 1041–1063. doi:10.1007/s10543-017-0659-8.

Naganawa, S., Sato, K., Katagiri, T., Mimura, T., Ishigaki, T., 2003. Regional adc values of the normal brain: differences due to age, gender, and laterality. European Radiology 13, 6–11. doi:10.1007/s00330-002-1549-1.

National Cancer Institute Clinical Proteomic Tumor Analysis Consortium (CPTAC), 2018. The clinical proteomic tumor analysis consortium cutaneous melanoma collection (cptac-cm) (version 11). doi:10.7937/K9/TCIA.2018.ODU24GZE.

Panda, A., Obmann, V.C., Lo, W.C., Margevicius, S., Jiang, Y., Schluchter, M., Patel, I.J., Nakamoto, D., Badve, C., Griswold, M.A., Jaeger, I., Ponsky, L.E., Gulani, V., 2019. Mr fingerprinting and adc mapping for characterization of lesions in the transition zone of the prostate gland. Radiology 292, 685–694. doi:10.1148/radiol.2019181705. epub 2019 Jul 23.

Perracchione, E., 2016. RBF-based partition of unity method: theory, algorithms and applications. Ph.D. thesis. University of Torino.

Perracchione, E., Massone, A.M., Piana, M., 2021. Feature augmentation for the inversion of the fourier transform with limited data. Inverse Problems 37, 105001. URL: https://doi.org/10.1088/1361-6420/ac1ad7, doi:10.1088/1361-6420/ac1ad7.

Rudin, L.I., Osher, S., Fatemi, E., 1992. Nonlinear total variation based noise removal algorithms. Physica D: nonlinear phenomena 60, 259–268. doi:10.1016/0167-2789(92)90242-F.

Rueckert, D., Sonoda, L.I., Hayes, C., Hill, D.L.G., Leach, M.O., Hawkes, D.J., 1999. Nonrigid registration using free-form deformations: Application to breast mr images. IEEE Transactions on Medical Imaging 18, 712–721. doi:10.1109/42.796284.

Rydelius, A., Bengzon, J., Engelholm, S., Kinhult, S., Englund, E., Nilsson, M., Lätt, J., Lampinen, B., Sundgren, P., 2023. Predictive value of diffusion mri-based parametric response mapping for prognosis and treatment response in glioblastoma. Magnetic Resonance Imaging 104, 88–96. doi:10.1016/j.mri.2023.09.005.

Sener, R.N., 2001. Diffusion mri: apparent diffusion coefficient (adc) values in the normal brain and a classification of brain disorders based on adc values. Computerized Medical Imaging and Graphics 25, 299–326. doi:10.1016/S0895-6111(00)00083-5.

Strong, D., Chan, T., 2003. Edge-preserving and scale-dependent properties of total variation regularization. Inverse problems 19, S165. doi:10.1088/0266-5611/19/6/059.

Tey, W.Y., Che Sidik, N.A., Asako, Y., W Muhieldeen, M., Afshar, O., 2021. Moving least squares method and its improvement: a concise review. Journal of Applied and Computational Mechanics 7, 883–889. doi:10.22055/jacm.2021.35435.2652.

Van Essen, D.C., Ugurbil, K., Auerbach, E., Barch, D., Behrens, T.E.J., Bucholz, R., Chang, A., Chen, L., Corbetta, M., Curtiss, S.W., Della Penna, S., Feinberg, D., Glasser, M.F., Harel, N., Heath, A.C., Larson-Prior, L., Marcus, D., Michalareas, G., Moeller, S., Oostenveld, R., Petersen, S.E., Prior, F., Schlaggar, B.L., Smith, S.M., Snyder, A.Z., Xu, J., Yacoub, E., 2012. The human connectome project: A data acquisition perspective. NeuroImage 62, 2222–2231. doi:10.1016/j.neuroimage.2012.02.018.

Weick, S., Breuer, K., Richter, A., Exner, F., Ströhle, S.P., Lutyj, P., Tamihardja, J., Veldhoen, S., Flentje, M., Polat, B., 2020. Non-rigid image registration of 4d-mri data for improved delineation of moving tumors. BMC Medical Imaging 20, 41. doi:10.1186/s12880-020-00439-6.

Wendland, H., 2004. Scattered data approximation. volume 17. Cambridge university press.

Woo, J., Stone, M., Prince, J.L., 2015. Multimodal registration via mutual information incorporating geometric and spatial context. IEEE Transactions on Image Processing 24, 757–769. doi:10.1109/TIP.2014.2387019.

Woodworth, D.C., Pope, W.B., Liau, L.M., Kim, H.J., Lai, A., Nghiemphu, P.L., Cloughesy, T.F., Ellingson, B.M., 2014. Nonlinear distortion correction of diffusion mr images improves quantitative dti measurements in glioblastoma. Journal of Neuro-Oncology 116, 551–558. doi:10.1007/s11060-013-1320-2. epub 2013 Dec 7.

Zhu, M., Yu, L., Wang, Z., Ke, Z., Zhi, C., 2023. A survey on objective evaluation of image sharpness. Applied Sciences 13, 2652. doi:10.3390/app13042652.